

---

# Report about Optimal back-projection for tomography

---

**Zhiping WANG**

MSc Student, Physics of Life

**Supervisor:** Dr. Ricardo Diogo Righetto and Dr. Valentin Debarn

April 28, 2025

## Contents

<b>1</b>	<b>INTRODUCTION</b>	<b>2</b>
<b>2</b>	<b>BACKGROUND</b>	<b>3</b>
2.1	Cryo-ET Data Acquisition and Projection Principles . . . . .	3
2.2	Fourier Central Slice Theorem and Reconstruction . . . . .	4
2.3	Filtered Back-Projection (FBP) Reconstruction . . . . .	4
2.4	Optimized FBP with Filter Design . . . . .	5
<b>3</b>	<b>METHOD</b>	<b>5</b>
3.1	Optimization of Filter . . . . .	5
3.2	Optimizer and Regularization . . . . .	6
3.2.1	AdamW Optimizer . . . . .	6
3.2.2	Total Variation (TV) Regularization . . . . .	7
3.2.3	Final Optimization Objective . . . . .	7
<b>4</b>	<b>RESULT</b>	<b>8</b>
4.1	Result with SHREC 2021 . . . . .	8
4.2	Results with real datasets . . . . .	9
4.2.1	Direct Interpolation . . . . .	9
4.2.2	Regenerating Projections . . . . .	10
<b>5</b>	<b>DISCUSSION</b>	<b>11</b>
5.1	Evolution of the Filter . . . . .	11
5.2	Limitations in Real Data Reconstruction . . . . .	14
5.3	Edge Blurring When Reducing Filter Dimensionality . . . . .	14
5.4	Effects of Radial Symmetry . . . . .	15
5.5	Overfitting and Excessive Denoising . . . . .	16
<b>6</b>	<b>Conclusion and Outlook</b>	<b>16</b>
<b>7</b>	<b>Acknowledgment</b>	<b>17</b>

# 1 INTRODUCTION

The exploration of the microscopic world and the pursuit of the fundamental principles of biophysics have driven our study of macromolecular structures in biology. In recent years, advancements in imaging techniques have enabled us to investigate biological structures at the nanometer scale. Among these techniques, cryo-electron microscopy (cryo-EM) has emerged as a powerful tool due to its ability to observe biological samples in near-native in situ conditions. Unlike traditional imaging methods, cryo-EM preserves the original state of biological macromolecules while providing high-resolution structural information, making it an invaluable technique in structural biology.

To meet the growing demand for three-dimensional (3D) structural analysis of biological macromolecules, several 3D imaging techniques have been developed, among which cryo-electron tomography (cryo-ET) is a prominent example. Cryo-ET reconstructs 3D structures by capturing a series of 2D projection images at different tilt angles and applying computational reconstruction methods. This technique enables the study of complex macromolecular assemblies in their native environments. However, reconstructing 3D structures from 2D projections is an ill-posed inverse problem, particularly in cryo-ET datasets, where high noise levels and limited angular coverage are common, posing significant challenges to accurate reconstruction [1].

Considering factors such as computational cost, processing time, and reconstruction accuracy, filtered back-projection (FBP) has become a widely used reconstruction technique in the field of cryo-ET due to its high computational efficiency. However, the quality of FBP reconstruction heavily depends on the choice of the filter, as different filters can affect both noise amplification and the preservation of structural features [3]. Therefore, in this study, we explore an optimized FBP approach that utilizes filter design tailored to the characteristics of cryo-ET data to enhance reconstruction accuracy and stability.

In this report, I will introduce the principles of cryo-ET, the mathematical background of the FBP reconstruction model, and the results obtained using optimized filters for reconstruction. Finally, I discuss several interesting phenomena encountered during the project, which are closely related to the reconstruction results.

## 2 BACKGROUND

### 2.1 Cryo-ET Data Acquisition and Projection Principles

Cryo-ET reconstructs 3D structures by acquiring a series of two-dimensional (2D) projections at different tilt angles. As illustrated in Figure 1, a vitrified sample is inserted into the cryo-TEM, where images are collected at incremental tilt angles, typically ranging from  $-60^\circ$  to  $+60^\circ$ . This tilt-series serves as the foundation for computational 3D reconstruction. However, practical limitations, such as sample holder geometry and radiation damage constraints, result in a missing wedge of information in Fourier space. This missing wedge leads to anisotropic resolution, causing distortions in the reconstructed tomogram, particularly along the tilt axis. Several approaches have been developed to mitigate the missing wedge problem, such as dual-axis tilt tomography [8], which involves acquiring a second tilt-series perpendicular to the first to improve Fourier space coverage. However, in this project, we focus solely on the single-axis tilt case, which remains the most commonly used setup due to its simplicity and lower electron dose exposure requirements.

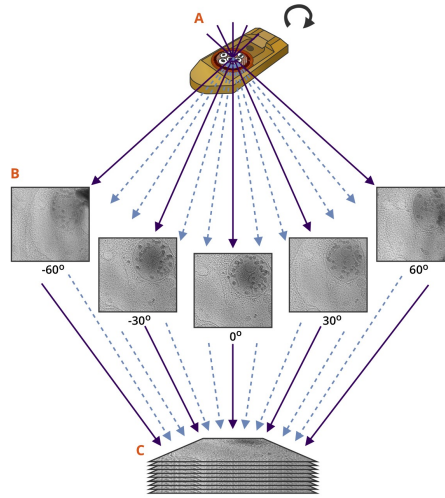


Figure 1: Workflow for Cryo-ET Image Acquisition. (A) The vitrified sample grid is inserted into the Cryo-TEM. (B) Images are collected at incremental tilt angles (typically between  $-60^\circ$  and  $+60^\circ$ ). (C) The tilt-series images are used to reconstruct the 3D tomogram. Source: [9]

The process of tomographic imaging can be mathematically described using the X-ray transform, which expresses the projection  $v(\vec{r}, \theta)$  of an unknown 3D sample density  $u(x, y, z)$  at a tilt angle  $\theta$ :

$$v(\vec{r}, \theta) = \int_{-\infty}^{\infty} u(z \cos(\theta) - \vec{r} \cdot \sin(\theta), z \sin(\theta) + \vec{r} \cdot \cos(\theta)) dz. \quad (1)$$

This integral equation, known as the **X-ray transform**, describes how 2D projections are generated from a 3D structure, forming the mathematical basis of tomographic reconstruction. (For 2D objects, such a transform is also equivalent to the Radon transform, to standardize terminology in 2D tomography.)

## 2.2 Fourier Central Slice Theorem and Reconstruction

A fundamental theorem in tomography is the Fourier Central Slice Theorem, which states that the 2D Fourier transform of a projection at a given tilt angle corresponds to a central slice of the 3D Fourier transform of the original object [6]. Mathematically, if we denote the Fourier transform of the 3D object as  $U(k_x, k_y, k_z)$ , then the Fourier transform of a projection  $V(k_x, k_y)$  at angle  $\theta$  satisfies:

$$V(k_x, k_y) = U(k_x, k_y \cos(\theta), k_y \sin(\theta)). \quad (2)$$

This means that each projection image contributes a single plane of information in Fourier space. By collecting multiple projections at different tilt angles, one can gradually fill the 3D Fourier space with planar slices. However, due to the limited tilt range, some regions of Fourier space remain unsampled, leading to the well-known missing wedge problem, which causes elongation artifacts in the final reconstruction.

To reconstruct the 3D volume from these Fourier slices, an inverse X-ray transform must be applied, which is typically achieved using FBP.

## 2.3 Filtered Back-Projection (FBP) Reconstruction

Filtered back-projection (FBP) is a widely used tomographic reconstruction method that leverages the Fourier slice theorem. It consists of two key steps:

- **Filtering:** Due to the central slice theorem, low-frequency components are oversampled, whereas high-frequency components are underrepresented. To compensate for this, a high-pass filter (such as the ramp filter or cosine filter) is applied to each projection before back-projection. This filtering operation is expressed as:

$$\hat{V}(k_x, k_y) = H(k_x, k_y)V(k_x, k_y), \quad (3)$$

where  $H(k_x, k_y)$  is a high-pass filter function.

- **Back-Projection:** After filtering, the projections are back-projected along their respective tilt angles to reconstruct the 3D volume. Mathematically, the reconstructed object  $\tilde{u}(\vec{r})$  is given by:

$$\tilde{u}(\vec{r}) = \int_{-\pi}^{\pi} \int_{\mathbb{R}} v(\vec{s}, \theta) h(n_{\theta} \cdot \vec{r} - \vec{s}) d\vec{s} d\theta. \quad (4)$$

Here,  $h$  represents the applied reconstruction filter, and  $n_{\theta} = (\cos(\theta), -\sin(\theta))^T$  is the tilt axis direction.

## 2.4 Optimized FBP with Filter Design

Traditional FBP is already a highly effective reconstruction method. In noise-free conditions, it produces excellent results, and even in the presence of noise, it remains sufficiently robust for practical use. However, we hypothesize that there is still room for improvement.

In this project, we propose an **optimized filtering approach** that takes into account the angular diversity of projections at different tilt angles. By refining the filtering strategy, we aim to enhance reconstruction quality by better preserving structural details and reducing artifacts associated with the limited angular coverage in Cryo-ET.

# 3 METHOD

## 3.1 Optimization of Filter

In this project, we assume that the reconstruction filter is an **optimizable parameter**, which can be learned through an iterative optimization process. Instead of using a fixed analytical filter (such as the Ram-Lak or cosine filter), we parameterize the filter and optimize it based on simulation data.

### Data Representation and Dimensions

We consider a 3D tomographic reconstruction problem, where the data representation is defined as:

- **Ground truth volume:**  $u \in \mathbb{R}^{z \times x \times y}$ , representing the underlying 3D structure.
- **Projection data (tilt-series):**  $y \in \mathbb{R}^{m \times x \times y}$ , where  $m$  is the number of tilt angles.
- **Filter parameterization:**  $\beta \in \mathbb{R}^{m \times x \times y}$ , representing a learnable 3D filter.
- **Reconstructed volume:**  $\hat{u}(\beta) \in \mathbb{R}^{z \times x \times y}$ , which is the output using optimal FBP.

The relationship between the projection data and the reconstructed volume follows:

$$y = \mathcal{X}(u, \theta) + \eta \quad (5)$$

This is the operator formulation of Eq. (1) incorporating noise, where:

- $\mathcal{X}$  is the **X-ray transform**, modeling the tomographic projection process.
- $\theta$  represents the tilt angles.
- $\eta$  is the noise in the measurement.

The FBP reconstruction with parameterized filtering is expressed as [5]:

$$\hat{u}(\beta) = \mathcal{X}^{-1}(y) = \text{FBP}(y, \beta) = \text{BP}(y * \beta) \quad (6)$$

where  $*$  represents convolution, and  $\beta$  is the learnable filter being optimized in spatial domain. To simplify computation in the subsequent training process, we chose to implement the filtering operation in the frequency domain. In this project, no padding is applied during the convolution operation. This may lead to boundary artifacts, which could be addressed in future work by incorporating an appropriate padding strategy.

## Optimization Process

The optimization is performed iteratively using gradient-based updates. Specifically, the gradient of the loss function with respect to the filter parameters  $\beta$  is computed via backpropagation.<sup>1</sup> We employ a first-order gradient-based optimizer (e.g., AdamW) to iteratively update the parameters.

## 3.2 Optimizer and Regularization

We optimize the reconstruction process using PyTorch, where the choice of optimizer plays a crucial role. Additionally, regularization significantly impacts the final reconstruction quality. To enhance the stability and effectiveness of the learned filter  $\beta$ , we adopt the AdamW optimizer and integrate TV regularization.

### 3.2.1 AdamW Optimizer

AdamW [10] is an improved version of the Adam optimizer that includes explicit weight decay for better generalization. The update rules are:

---

<sup>1</sup>This subsection was refined with suggestions from ChatGPT (OpenAI, version 3.5, accessed on March 1, 2025).

$$m_t = \beta_1 m_{t-1} + (1 - \beta_1) \nabla_\beta L, \quad v_t = \beta_2 v_{t-1} + (1 - \beta_2) (\nabla_\beta L)^2 \quad (7)$$

$$\hat{m}_t = \frac{m_t}{1 - \beta_1^t}, \quad \hat{v}_t = \frac{v_t}{1 - \beta_2^t} \quad (8)$$

$$\beta \leftarrow \beta - \alpha \frac{\hat{m}_t}{\sqrt{\hat{v}_t} + \epsilon} - \lambda \beta \quad (9)$$

where  $\lambda$  represents weight decay.

### 3.2.2 Total Variation (TV) Regularization

To enforce smoothness while preserving structural details, we introduce TV regularization, which penalizes sharp variations in the learned filter. The discrete isotropic total variation is formulated as [7]:

$$L_{\text{TV}} = \sum_{i,j,k} (|\beta_{i+1,j,k} - \beta_{i,j,k}| + |\beta_{i,j+1,k} - \beta_{i,j,k}| + |\beta_{i,j,k+1} - \beta_{i,j,k}|) \quad (10)$$

which represents the sum of absolute first-order gradients in different spatial directions.

Alternatively, the continuous formulation of TV regularization is given by:

$$L_{\text{TV}} = \|\nabla \beta\| \quad (11)$$

By incorporating TV regularization, we effectively reduce noise while maintaining important structural features, ensuring an optimal balance between smoothness and detail preservation in the learned filter.

### 3.2.3 Final Optimization Objective

The total loss function combines data fidelity, sparsity, and smoothness constraints:

$$L_{\text{total}} = L_{\text{MSE}} + \lambda_{\text{TV}} \cdot L_{\text{TV}} \quad (12)$$

where the mean squared error (MSE) loss is:

$$L_{\text{MSE}} = \frac{1}{n^3} \sum_{i,j,k} \|\hat{u}_{i,j,k}(\beta) - u_{i,j,k}\|^2 \quad (13)$$

The optimization follows by Eq. 9.



This approach ensures an optimal balance between noise suppression, reconstruction accuracy, and computational efficiency.

## 4 RESULT

### 4.1 Result with SHREC 2021

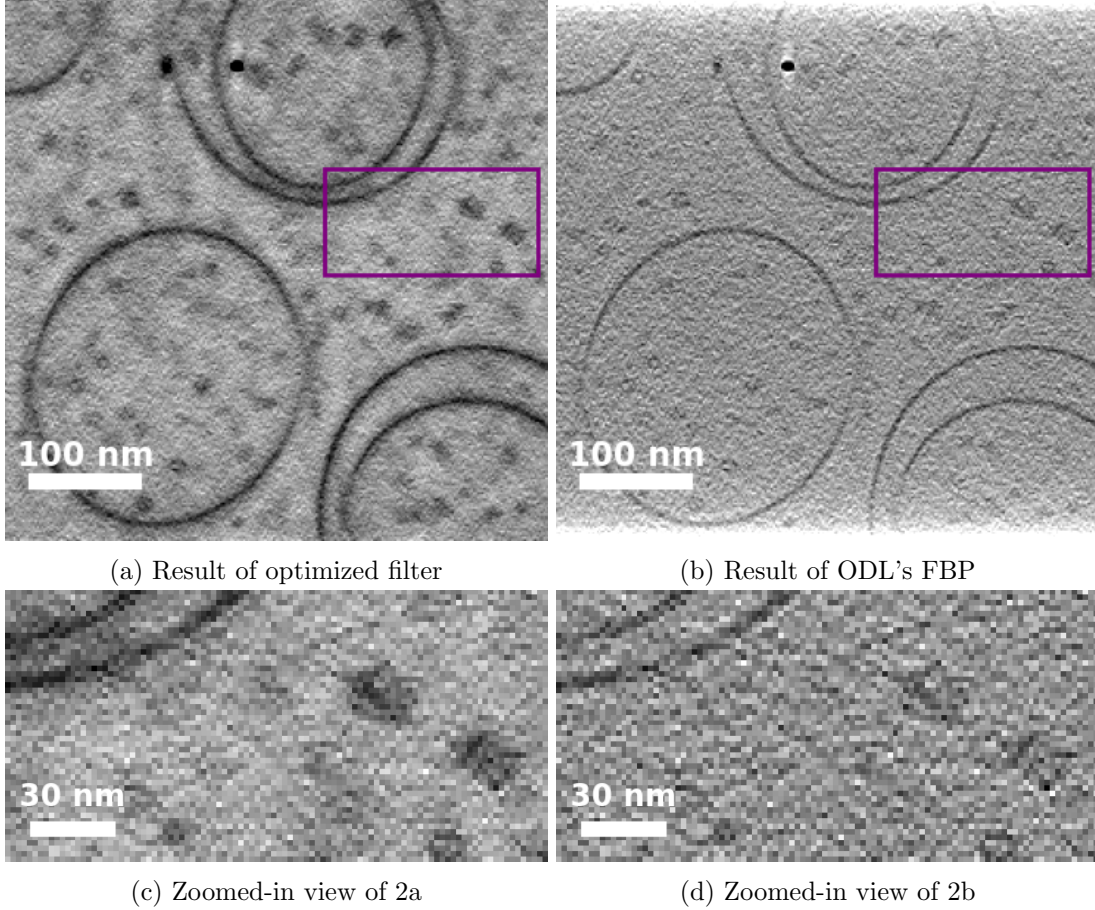


Figure 2: Reconstruction results of the SHREC noise dataset at the central slice.

SHREC 2021 is a simulated Cryo-ET dataset with a tilt range of  $-60^\circ$  to  $+60^\circ$ , containing 61 projection images per sample and 10 different models. Since this dataset is simulated, it provides ground truth reconstructions, enabling direct training using the proposed method [2].

For training, we used models 1 to 9, while model 0 was reserved for testing. Due to hardware constraints, the original data size of  $360 \times 1024 \times 1024$  was downsampled to  $90 \times 256 \times 256$ .

To accelerate training and enhance stability, we adopted the ramp filter as the initial guess. The optimized filter was then applied in the reconstruction process using ODL's back-projection operator and compared with the standard FBP function from ODL. Simultaneously, we em-

ployed the following loss function:

$$L = \mathcal{L}(\hat{u}, u) + \lambda_{TV} \cdot TV(\hat{u}) \quad (14)$$

where  $L$  is the overall loss function,  $\mathcal{L}$  is the Huber loss, and  $\lambda_{TV}$  is the coefficient for the TV regularization term.

The reconstruction results are shown in Fig. 2.

As previously mentioned, the FBP reconstruction using ODL already provides sufficiently good results, demonstrating high-quality reconstructions. The optimized filter achieves comparable results while enhancing contrast, though with a slight reduction in resolution. Regularization further reduces noise, leading to a smoother reconstruction and sharper contrast.

## 4.2 Results with real datasets

Real data differ significantly from the SHREC dataset in several key aspects, including pixel size, sampling environment, and sensor physical properties (e.g., the modulation transfer function, MTF). Relying solely on the SHREC training dataset thus presents substantial challenges. The most critical issue is the difference in tilt angles: our real dataset—a *Chlamydomonas* sample from EMPIAR-11830—comprises 35 tilt angle projections [4], whereas the SHREC dataset contains 61 angles and operates within a distinct numerical range. Consequently, the filter optimized on the SHREC dataset is unsuitable for direct application to the real sample. To address this discrepancy, two approaches were explored:

### 4.2.1 Direct Interpolation

The simplest approach is to use interpolation algorithms to obtain tilt angles that were not originally considered. By applying linear interpolation using various methods, we can generate the required angles, thereby resolving the issue of differing tilt angles between the training set and real-world scenarios. Among the various interpolation techniques tested, the 4th-order polynomial least squares method performed best on this dataset. The results are in Fig 3.

Unfortunately, although this method effectively enhanced contrast to some extent, it also significantly increased blurring and introduced non-uniform background artifacts, resulting in a suboptimal reconstruction.

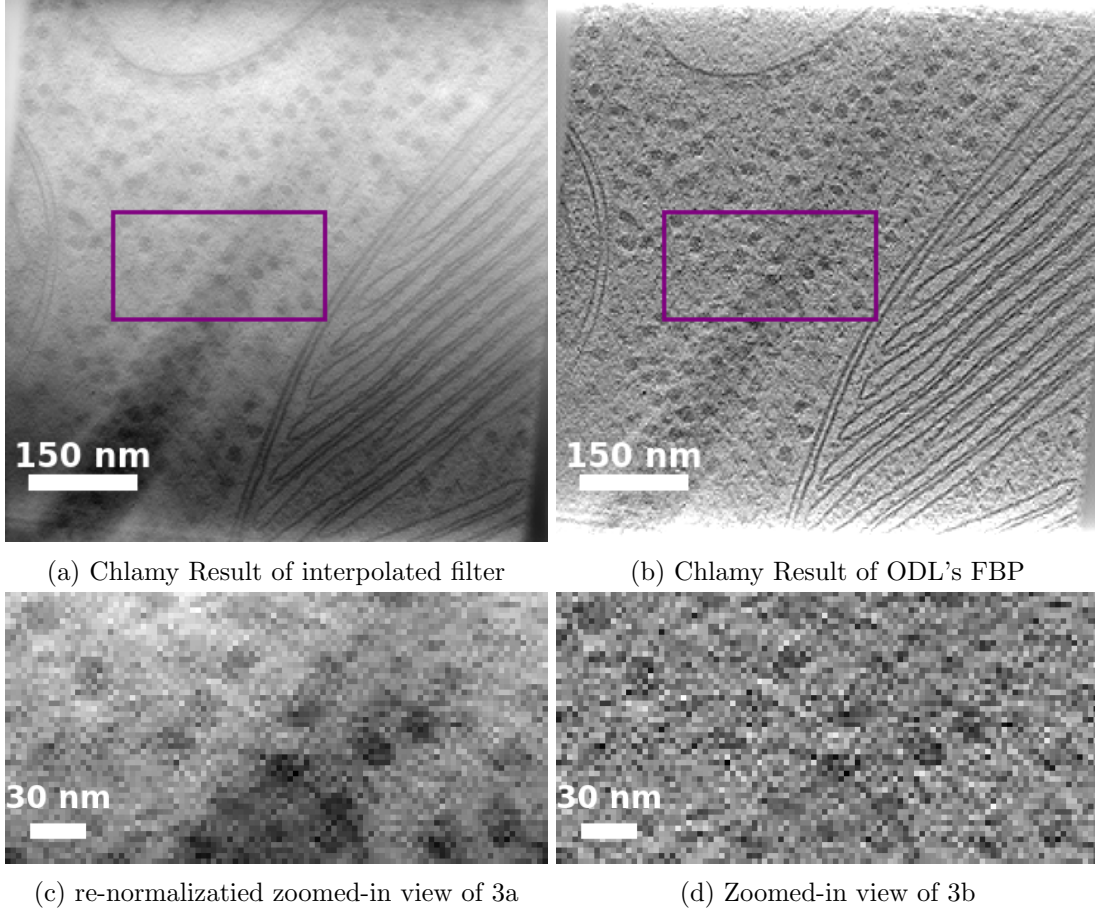


Figure 3: Reconstruction results of the SHREC noise dataset at the central slice.

#### 4.2.2 Regenerating Projections

Since the SHREC dataset is itself simulated, we can regenerate a series of projections that match the tilt angles of the real sample based on the ground truth volume. This approach enables us to obtain a filter that is better suited for real data. However, directly regenerating projections in this manner introduces additional mismatches between the model and the data, leading to severe ghosting artifacts and non-uniformity. To address these issues, we incorporated regularization terms tailored to real data into the optimization process. After comparing several options, the following loss function was chosen:

$$L = \mathcal{L}(\hat{u}, u) + \lambda_{TV_1} \cdot TV(\hat{u}) + \lambda_{TV_2} \cdot TV(\beta * y) \quad (15)$$

where  $L$  is the overall loss function,  $\mathcal{L}$  is the Huber loss, and  $*$  denotes convolution, indicating that we filter the projections using the filter  $\beta$ . We apply TV regularization separately to the filtered projections and the reconstructions, with the corresponding coefficients  $\lambda_{TV_1}$  and  $\lambda_{TV_2}$ , respectively.

The final results are shown in Fig. 4. We observed that whether the filter was optimized or the reconstruction was directly performed using ODL, the performance was nearly identical, with no significant improvements in reconstruction quality.

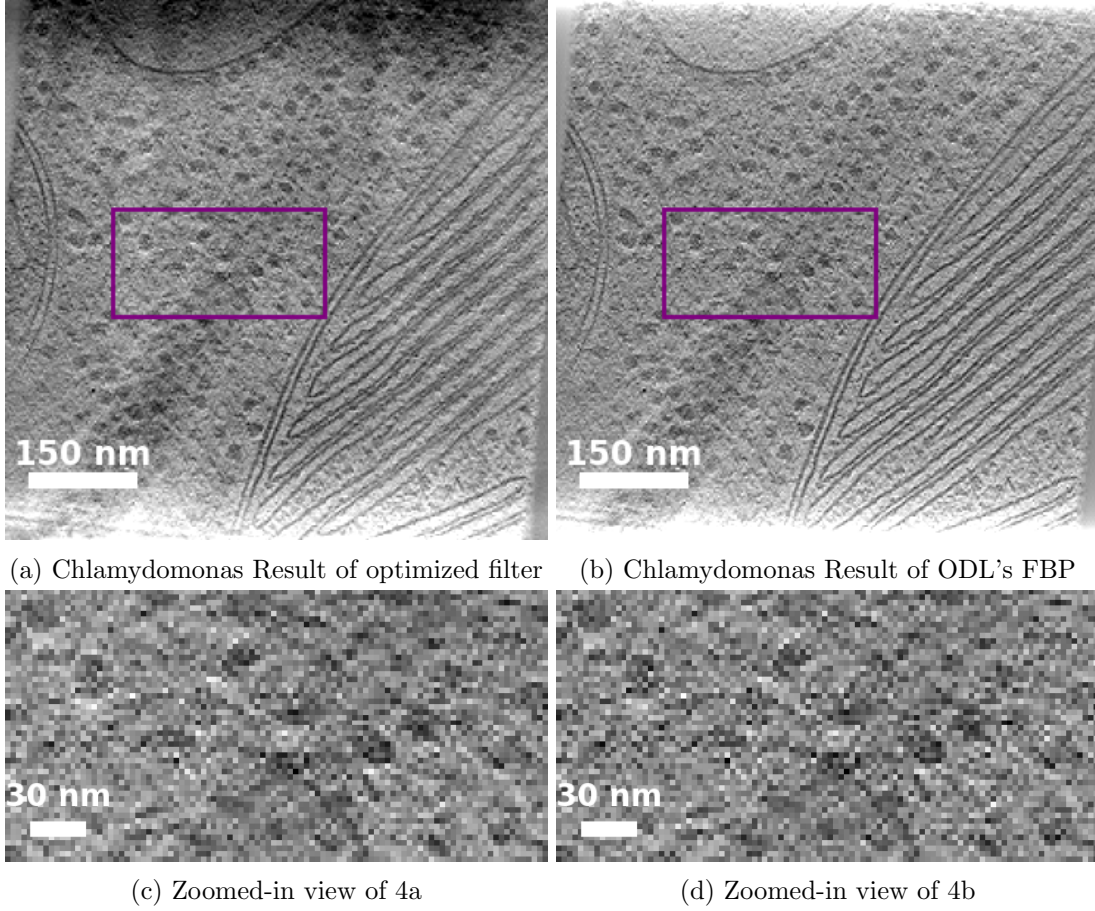


Figure 4: Reconstruction results of the SHREC noise dataset at the central slice.

## 5 DISCUSSION

Throughout this project, several intriguing phenomena were observed, whose solutions and implications are worth discussing. This section explores these key aspects in detail.

### 5.1 Evolution of the Filter

In FBP reconstruction, the filter directly influences the final image quality. Our study demonstrates that while the Ramp filter serves as the best initial guess (see Fig. 5), the optimized filter undergoes significant modifications in the low-frequency region. These adjustments enhance image contrast, bringing the reconstruction closer to the ground truth.

As shown in Fig. 6, the optimized filter, derived from training on the SHREC dataset, deviates from the standard Ramp filter in the low-frequency range. This deviation indicates

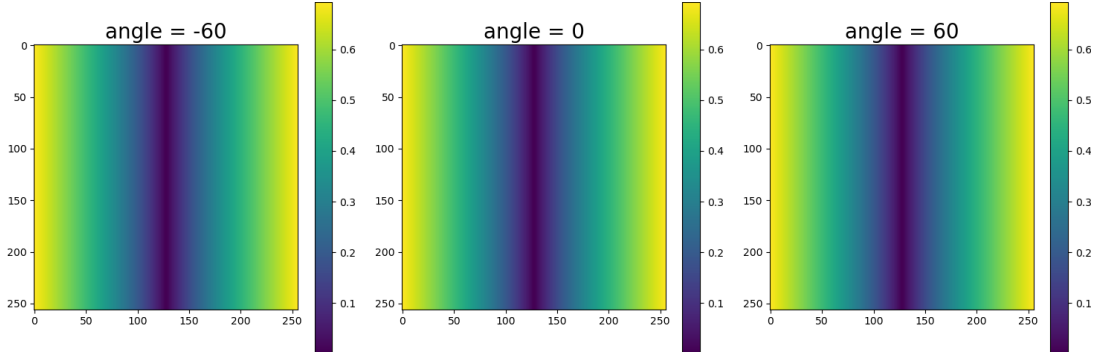


Figure 5: Initial Ramp Filter

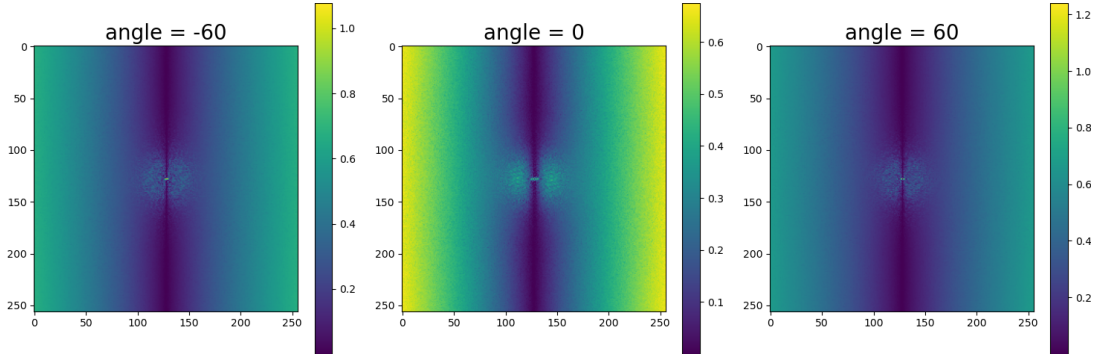


Figure 6: Optimized Filter from the SHREC Dataset

that the optimization process redistributes frequency components to better match the characteristics of Cryo-ET data. By preserving more low-frequency information, the optimized filter improves contrast and structural visibility, whereas the Ramp filter's strong suppression of these components can lead to a flattened intensity distribution and reduced contrast.

For real data, the number of tilt angles changes. The interpolated filter—generated to adjust for the different angles—closely resembles that of the SHREC dataset since it is merely interpolated. This approach may lead to imperfect training and imprecise interpolation, resulting in suboptimal clarity and background uniformity.

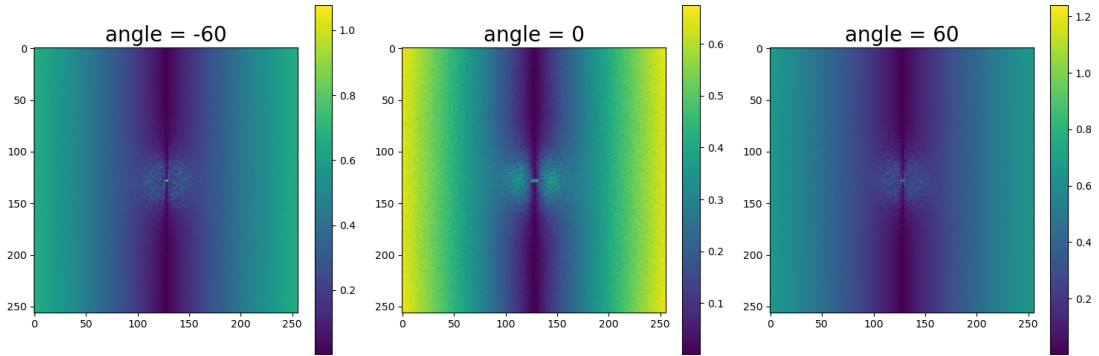


Figure 7: Interpolated Filter for Real Data

In contrast, the filter obtained via regenerating synthetic projections—with the inclusion of



additional regularization—exhibits distinct characteristics, such as noticeable horizontal streaks. These differences underscore the inconsistency between the real data and the SHREC dataset, and they highlight the need for more comprehensive datasets to develop a universally applicable filter.

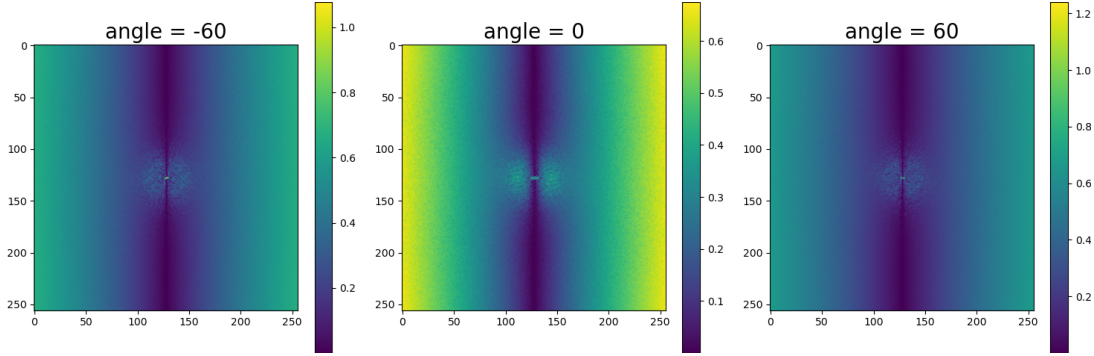


Figure 8: Retained Filter from Regenerated Projections for Real Data

For a direct comparison, we plotted the normalized radial profiles (see Fig. 9) to contrast the different filters. It can be observed that starting from the ramp filter (red), all filters undergo some modifications. Due to the nature of the interpolation process, the interpolated filter completely overlaps with the filter from the SHREC dataset. Additionally, the retrained filter does not exhibit significant improvements in the low-frequency range, possibly because the regenerated projections deviate substantially from real conditions, which might explain its limited ability to enhance contrast.

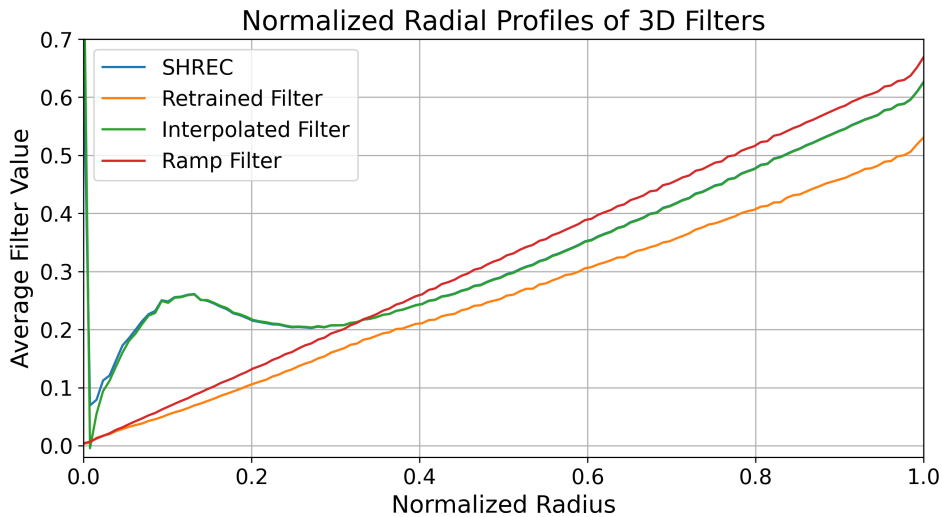


Figure 9: Normalized radial profiles of 3D filters (SHREC, Retrained, Interpolated, and Ramp) plotted over a normalized radius

## 5.2 Limitations in Real Data Reconstruction

The reconstruction results on real data reveal clear limitations compared to conventional methods. While the outcomes are not entirely erroneous, they fall short of optimal performance. This shortfall can be attributed to several factors: the model was trained exclusively on synthetic data, which introduces a domain shift when applied to real data lacking ground truth; differences in pixel size and noise characteristics between the simulated and real datasets further exacerbate the problem; the limited size of the training set restricts the model’s generalizability; and the optimized filter, being directional rather than isotropic, fails to capture the full range of real data variations. In summary, these challenges underscore the need for improved datasets, larger training sets, and more advanced methods to bridge the gap between simulated and real-world imaging conditions.

## 5.3 Edge Blurring When Reducing Filter Dimensionality

Another interesting observation is the appearance of edge blurring when reducing the dimensionality of the filter. Initially, to reduce memory consumption, we formulated the reconstruction model as

$$\hat{u}(\beta) = \mathcal{BP}(\beta_1 * \beta_2 * y) \quad (16)$$

where  $\beta_1 \in \mathbb{R}^m$  is a one-dimensional filter acting along the tilt angle, and  $\beta_2 \in \mathbb{R}^{x \times y}$  is a two-dimensional filter acting in the camera plane.

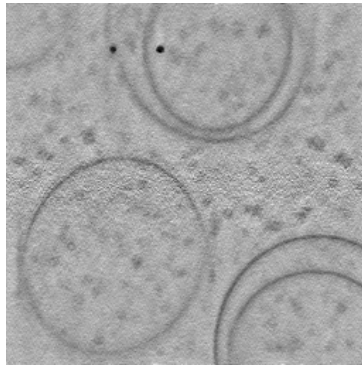


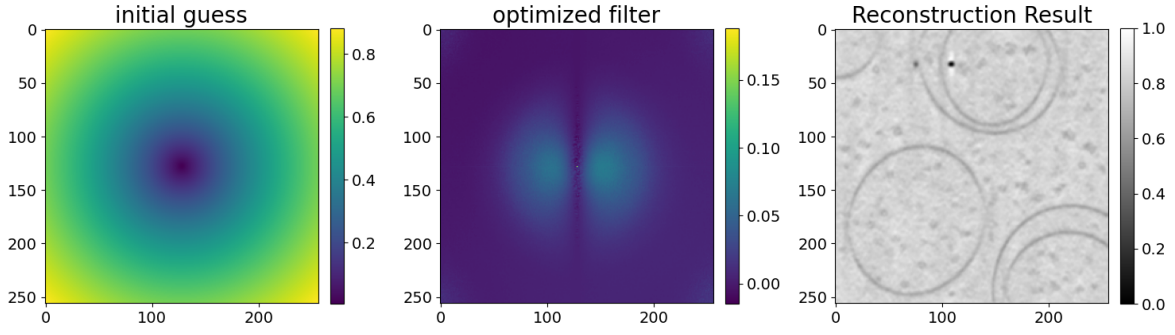
Figure 10: Illustration of edge blurring

During experiments, it was observed that when retaining only the one-dimensional filter, significant edge blurring occurred, as shown in Fig. 10. However, when using only the two-dimensional filter while restricting updates to the one-dimensional filter, the results became acceptable, although still inferior to those obtained with a fully three-dimensional filter. This

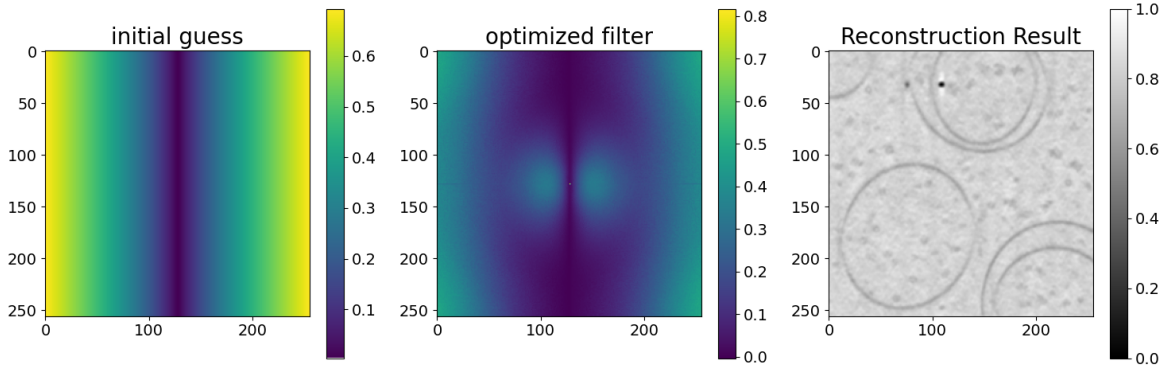
phenomenon is currently believed to stem from an incomplete model representation, where the one-dimensional filter did not receive sufficient training, leading to suboptimal performance.

#### 5.4 Effects of Radial Symmetry

In our previous discussion on edge blurring, the filters  $\beta_2$  were initially based on a 1D ramp filter, and the final results were not rotationally symmetric. Therefore, we adopted a rotationally symmetric filter as the initial guess, suspecting that this might be the cause of the blurring. Later, after testing with a radial filter, we found that this is not the fundamental reason for the blurring, although the comparison remains interesting. To mitigate the edge blurring effect, we fixed  $\beta_1$  (i.e., only used a 2D  $\beta_2$  for training), and the results are shown in the figure below.



(a) Rotationally symmetric filter initialization



(b) 1D ramp filter initialization

Figure 11: Filter initialization: The rotationally symmetric filter yields more isotropic results, while the 1D ramp filter produces more anisotropic results.

We can observe that, after training, the rotationally symmetric filter tends to yield more isotropic (uniform) results, whereas the 1D ramp filter initialization produces more anisotropic outcomes. Due to time constraints, the filter was only tested in 2D, yet some differences are still evident. We look forward to further analysis of initialization and rotational symmetry in future work.



## 5.5 Overfitting and Excessive Denoising

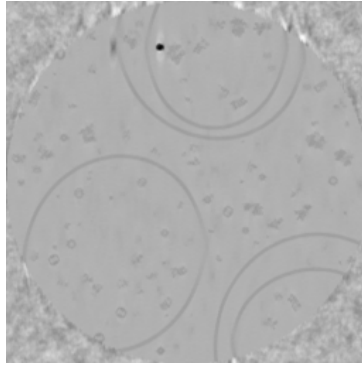


Figure 12: Illustration of overfitting effects

At the early stages of this study, reconstructions often exhibited excessively strong denoising effects, which initially appeared promising. However, further analysis revealed that this was primarily due to overfitting during training.

As shown in Fig. 12, an overly smooth region is present in the center, completely devoid of noise. This excessive smoothing indicates overfitting and provides no meaningful guidance for reconstruction.

This issue was particularly evident when a zero filter was used as the initial guess. The zero filter significantly disrupted the learning process, leading to an over-smoothed reconstruction where fine details were lost. To mitigate this, the Ramp filter was later adopted as the initial guess, resulting in more stable and robust reconstructions while reducing errors caused by overfitting.

## 6 Conclusion and Outlook

In this study, we developed an optimized filtered back-projection (FBP) approach for cryo-electron tomography by parameterizing the reconstruction filter and refining it through an iterative optimization process on simulated data from the SHREC dataset. Our results demonstrated that adjusting the low-frequency components of the filter can enhance image contrast and improve structural visibility. However, applying the optimized filter directly to real data—specifically, a *Chlamydomonas* sample from EMPIAR-11830—revealed substantial challenges. The discrepancies in tilt angles, pixel size, noise characteristics, and sensor properties between the synthetic and real datasets significantly limit the performance of the optimized filter.

Two approaches were explored to address these issues: direct interpolation to adjust for

differing tilt angles and regenerating synthetic projections that better match the real data. While both methods yielded reconstruction results that were comparable to those produced by conventional FBP, they also introduced artifacts such as blurring and non-uniform backgrounds, highlighting the inherent difficulties in bridging the domain gap.

Looking ahead, future work should focus on acquiring and integrating larger, more diverse datasets to better capture the variability in real-world imaging conditions. Additionally, it is essential to comprehensively consider the experimental environment, preprocessing methods, and additional physical constraints. By exploring isotropic filter designs and combining these elements with more advanced and practical optimization strategies, we anticipate achieving significantly improved reconstruction results.

## 7 Acknowledgment

This is my first Master's project at the Biozentrum, carried out from November 2024 to February 2025 in the lab of Prof. Dr. Benjamin Engel and lab of Prof. Dr. Ivan Dokmanić. I am deeply grateful to Dr. Ricardo Diogo Righetto, Vinith Kishore, and Dr. Valentin Debern for their detailed guidance, debugging assistance, insightful ideas, and valuable suggestions. I would also like to thank my colleagues from both labs for their constructive discussions, questions, and feedback during my presentations, which helped highlight some of the project's shortcomings and areas that required further consideration.

Portions of the language editing and content refinement in this report were assisted by ChatGPT (OpenAI, version 3.5, accessed on March 16, 2025).

## References

- [1] Simon Arridge, Peter Maass, Ozan Öktem, and Carola-Bibiane Schönlieb. Solving inverse problems using data-driven models. *Acta Numerica*, 28:1–174, 2019.
- [2] Ilja Gubins, Marten L Chaillet, Gijs van Der Schot, Remco C Veltkamp, Friedrich Förster, Yu Hao, Xiaohua Wan, Xuefeng Cui, Fa Zhang, Emmanuel Moebel, et al. Shrec 2020: Classification in cryo-electron tomograms. *Computers & Graphics*, 91:279–289, 2020.
- [3] George Harauz and Marin van Heel. Exact filters for general geometry three dimensional reconstruction. *Optik.*, 73(4):146–156, 1986.
- [4] Ron Kelley, Sagar Khavnekar, Ricardo D Righetto, Jessica Heebner, Martin Obr, Xianjun Zhang, Saikat Chakraborty, Grigory Tagiltsev, Alicia K Michael, Sofie van Dorst, et al. Towards community-driven visual proteomics with large-scale cryo-electron tomography of *chlamydomonas reinhardtii*. *bioRxiv*, pages 2024–12, 2024.
- [5] Sin Kim, Anil Kumar Khambampati, and Kyung Youn Kim. Mathematical concepts for image reconstruction in tomography. In *Industrial Tomography*, pages 335–387. Elsevier, 2022.
- [6] Aaron Klug and Richard Anthony Crowther. Three-dimensional image reconstruction from the viewpoint of information theory. *Nature*, 238(5365):435–440, 1972.
- [7] Zhenwei Luo, Adam A Campos-Acevedo, Longfei Lv, Qinghua Wang, and Jianpeng Ma. Sparseness and smoothness regularized imaging for improving the resolution of cryo-em single-particle reconstruction. *Proceedings of the National Academy of Sciences*, 118(2):e2013756118, 2021.
- [8] Alexander G Myasnikov, Zhanna A Afonina, and Bruno P Klaholz. Single particle and molecular assembly analysis of polyribosomes by single-and double-tilt cryo electron tomography. *ultramicroscopy*, 126:33–39, 2013.
- [9] MyScope Training. Data Acquisition in Cryo-Electron Tomography, 2023. Accessed: 2023-01-29.
- [10] PyTorch Contributors. Adamw optimizer - pytorch documentation, 2024. Accessed: 2024-02-24.